

Redox-Controlled conductance of polyoxometalate molecular junctions.

Cécile Huez,¹ David Guérin,¹ Stéphane Lenfant,¹ Florence Volatron,² Michel Calame,^{3,4} Mickael L. Perrin,^{3,5} Anna Proust² and Dominique Vuillaume.¹

1) Institute for Electronics Microelectronics and Nanotechnology (IEMN), CNRS, University of Lille, Av. Poincaré, Villeneuve d'Ascq, France.

2) Institut Parisien de Chimie Moléculaire (IPCM), CNRS, Sorbonne Université, 4 Place Jussieu, F-75005 Paris, France.

3) EMPA, Transport at the Nanoscale Laboratory, 8600 Dübendorf, Switzerland.

4) Dept. of Physics and Swiss Nanoscience Institute, University of Basel, Klingelbergstrasse 82, 4056 Basel, Switzerland.

5) Department of Information Technology and Electrical Engineering, ETH Zurich, 8092 Zurich, Switzerland.

SUPPORTING INFORMATION

Section 1. Synthesis and characterization of (TBA)₃[PMo^{VI}₁₂O₄₀] (PMo₁₂(0)) and (TBA)₄[PMo^{VI}₁₁Mo^V₁O₄₀] (PMo₁₂(I)).

PMo₁₂(0) and PMo₁₂(I) have been synthesized according to previously published procedures.^{1, 2} The purity of the compounds was confirmed by IR and ³¹P NMR spectroscopies.

Synthesis of PMo₁₂(0): 60 mL of a 1M solution of sodium molybdate dihydrate Na₂[MoO₄].2H₂O was added to 9 mL of nitric acid HNO₃ and 50 mL of 1,4-

dioxane. Under stirring, 5 mL of a 1 M solution of orthophosphoric acid H_3PO_4 and 5g of tetrabutylammonium bromide NBu_4Br (TBABr) are added. After filtration, the yellow heavy solid is immersed in 50 mL of boiling water and stirred, filtered again and washed with 50 mL water, 100 mL ethanol and diethyl ether until obtaining a yellow powder. It is finally recrystallized in hot acetone: 30 mL of hot acetone are required to recrystallize 1 g of powder. After three days in the refrigerator, the mixture is filtered and yellow crystals are collected, dried under vacuum several days at 60°C . Note that during the experiment, the POM was handled with glass spatula/material to avoid its reduction. IR (KBr, cm^{-1}): 2962 (m), 2933 (m), 2873 (m), 1473 (m), 1381 (w), 1063 (s), 967 (shoulder), 956 (vs), 880 (s), 806 (vs), 739 (w), 619 (w), 504 (m), 465 (w), 387 (s), 342 (m). ^{31}P NMR (400 MHz, CD_3CN , ppm): $\delta = -3.29$ (s).

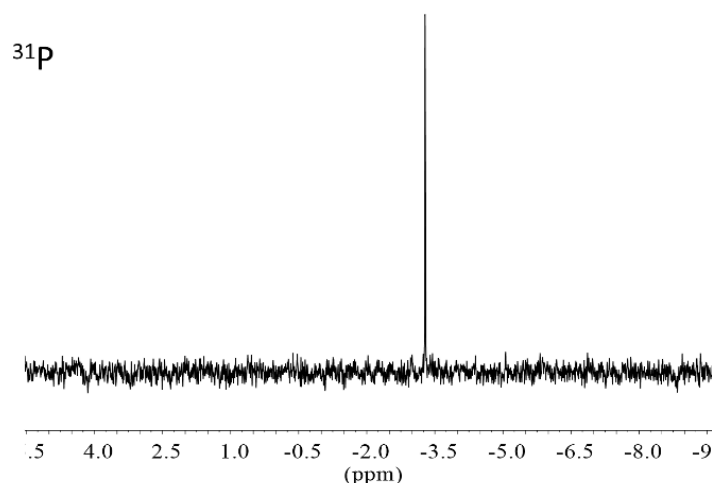


Figure S1. ^{31}P NMR spectrum of $\text{PMo}_{12}(\text{O})$ recorded in CD_3CN .

Synthesis of $\text{PMo}_{12}(\text{I})$: 100 mg of $(\text{TBA})_3[\text{PMo}_{12}\text{O}_{40}]$ are dissolved in a minimum volume of dry acetonitrile (~6 mL) in a dry Schlenk tube containing a magnetic stir bar, under Argon. Under stirring, a few drops of phenyllithium are added to the $\text{PMo}_{12}(\text{O})$ solution (color change from yellow to green). The reaction is

followed by recording ^{31}P NMR spectra in which the initial singlet at -3.29 ppm slowly disappears. Drops of phenyllithium is added until the appearance of a signal at 0.49 ppm corresponding to $\text{PMo}_{12}(\text{I})$, and the solution displays a blue color. 15 mg of NBu_4Br are added to the solution followed by the addition of ~ 15 mL of diethylether, leading to the formation of a blue precipitate. The suspension is filtered on a cellulose membrane. The blue solid is subsequently washed with 10 mL of tetrahydrofuran and 10 mL of methanol. It is finally dried under vacuum, in the dark. ^{31}P NMR (162 MHz, CD_3CN , ppm): $\delta = 0.49$ (s).

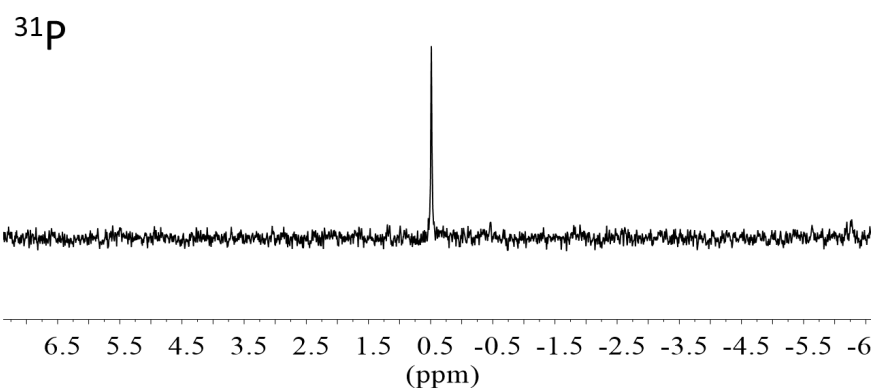


Figure S2. ^{31}P NMR spectrum of $\text{PMo}_{12}(\text{I})$ recorded in CD_3CN .

The electrochemical behavior of a 1 mM solution of $(\text{TBA})_3[\text{PMo}^{\text{VI}}_{12}\text{O}_{40}]$ in 0.1 M TBAPF_6 in CH_3CN was checked by cyclic voltammetry. A standard three electrode cell was used, which consisted of a working vitreous carbon electrode, an auxiliary platinum electrode and an aqueous saturated calomel electrode (SCE) equipped with a double junction to allow its use in an organic solvent. In those conditions the redox potential can be equally given versus SCE (0.308 V versus NHE) or recalculated versus the Fc^+/Fc couple (0.690 V versus NHE).³ The cyclic voltammogram is displayed below (Fig. S3). It features three reversible monoelectronic processes with midpoint potentials $E_{1/2} = 0.5(E_{\text{pa}} - E_{\text{pc}})$ (E_{pa} : anodic peak potential; E_{pc} cathodic peak potential) at $+0.142$, -0.272 and -0.991 V/SCE

(respectively -0.24, -0.654 and -1.373 V versus Fc^+/Fc). The LUMO energy position is calculated by $E_{\text{LUMO}} = -(E_{1/2\text{red}} + E_{\text{ref/ESH}}) - 4.44$, with $E_{\text{ref/ESH}} = 0.308$ eV for the saturated calomel electrode (SCE) in CH_3CN . With $E_{1/2\text{red}} = 0.142$ V/SCE for the one-electron reduction, we get $E_{\text{LUMO}} = -4.89$ eV with respect to the vacuum level.

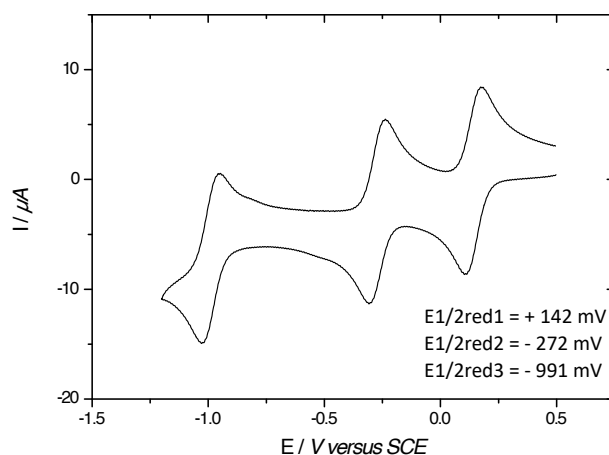


Figure S3. Cyclic voltammetry showing reduction of the PMo_{12} up to 3 electrons.

The redox state was also characterized by UV-vis spectroscopy of POMs in solution ($\approx \mu\text{M}$ in CH_2Cl_2). UV-Vis absorption spectra (Fig. S4) were recorded on a Lambda 800 Perkin-Elmer spectrometer. For the reduced $\text{PMo}_{12}(\text{I})$, we clearly observe a shift of the LMCT (ligand-to-metal charge transfer) band ($309 \rightarrow 315$ nm) and the appearance of the IVCT (intervalence charge transfer) band between Mo(V) and Mo(VI) at around 750 nm.

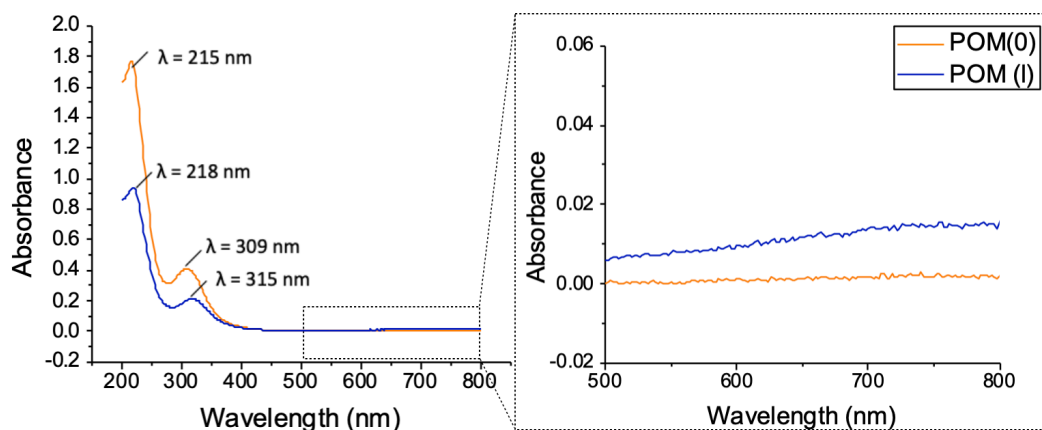


Figure S4. UV-vis absorbance spectra of $PMo_{12}(O)$ and $PMo_{12}(I)$ in solution.

High resolution XPS spectra were recorded with a monochromatic $Al_{K\alpha}$ X-ray source ($h\nu = 1486.6$ eV), a detection angle of 45° as referenced to the sample surface, an analyzer entrance slit width of $400 \mu m$ and with an analyzer pass energy of 12 eV. In these conditions, the overall resolution as measured from the full-width half-maximum (FWHM) of the Ag $3d_{5/2}$ line is 0.55 eV. Background was subtracted by the Shirley method.⁴ The peaks were decomposed using Voigt functions and a least squares minimization procedure. Binding energies (BE) were referenced to the C 1s BE, set at 284.8 eV. The XPS measurements were done on powder of $PMo_{12}(O)$ and $PMo_{12}(I)$ deposited on Si/SiO₂ functionalized with APTES (aminopropyltriethoxysilane) that give a better uniform deposition of the powder than on Au functionalized with aminoalkylthiol. The figure S5 shows the Mo 3d spectra. The energy splitting between the 3d $3/2$ and 3d $5/2$ peaks is fixed to 3.15 eV with an amplitude ratio of 0.67.⁵ From the peak areas, we calculate the Mo(VI)/Mo(V) ratios of 12.1 for $PMo_{12}(O)$ and 3.9 for $PMo_{12}(I)$.

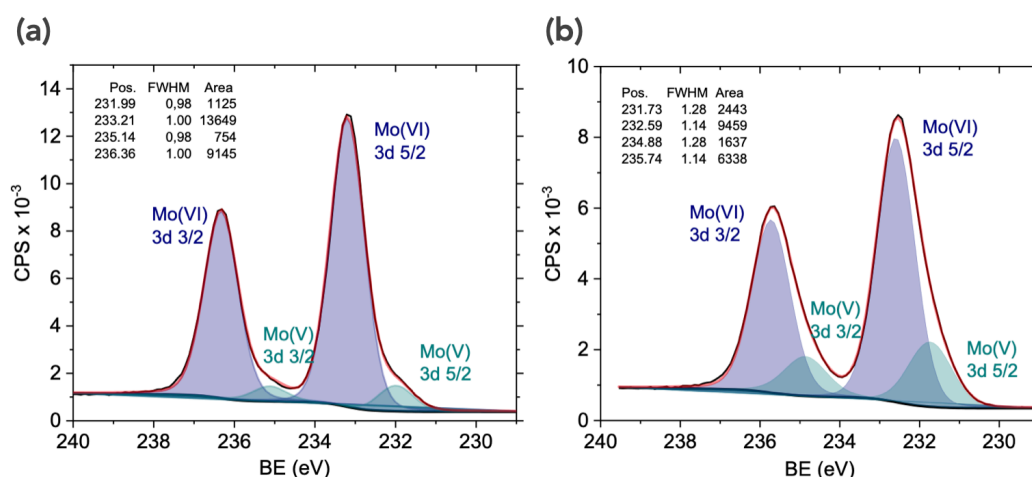


Figure S5. XPS spectra (Mo 3d) of (a) PMo₁₂(O) and (b) PMo₁₂(I).

Section 2. Electrodes and SAMs fabrication.

Electrodes.

Ultraflat template-stripped gold surfaces (^{TS}Au), with rms roughness of ~0.4 nm were prepared according to the method already reported.⁶⁻⁸ In brief, a 300–500 nm thick Au film was evaporated on a very flat silicon wafer covered by its native SiO₂ (rms roughness of ~0.4 nm), which was previously carefully cleaned by piranha solution (30 min in 7:3 H₂SO₄/H₂O₂ (v/v); **Caution:** Piranha solution is a strong oxidizer and reacts exothermically with organics), rinsed with deionized (DI) water, and dried under a stream of nitrogen. Clean 10x10 mm pieces of glass slide (ultrasonicated in acetone for 5 min, ultrasonicated in 2-propanol for 5 min, and UV irradiated in ozone for 10 min) were glued on the evaporated Au film (UV-polymerizable glue, NOA61 from Epotecnycy), then mechanically peeled off providing the ^{TS}Au film attached on the glass side (Au film is cut with a razor blade around the glass piece).

Self-assembled monolayers.

The self-assembled monolayers (SAMs) of 6-aminohexane-1-thiol (HS-(CH₂)₆-NH₂) were prepared following a protocol optimized and described in a previous work

for the electrostatic immobilization of POMs on amine-terminated SAMs.⁹ The freshly prepared ¹⁹⁷Au substrates were dipped in a solution of 6-aminohexane-1-thiol hydrochloride (Sigma-Aldrich) at a concentration of 10⁻³ M in ethanol overnight in the dark. The samples were rinsed in ethanol for 5 min and then ultrasonically cleaned 5 min in deionized (DI) water. These SAMs were treated by a PBS (phosphate-buffered saline, pH=7.4) solution for 2 hours, followed by ultrasonication in DI water for 5 minutes. The substrates were finally washed with ethanol and dried under nitrogen flow. It was found that the PBS treatment removes the formation of aggregates on the aminoalkylthiol SAMs as well as avoids clustering of POMs during the electrostatic deposition, likely because this treatment optimizes the ratio of NH₃⁺/NH₂ on the surface.⁹ The electrostatic deposition of PMo₁₂(O) and PMo₁₂(I) was done by immersion of these SAMs in a solution of PMo₁₂ at a concentration of 10⁻³ M in acetonitrile for one to few hours. We checked by ellipsometry that the thickness of the POM layer was independent of the immersion time when the immersion time is longer than 1h. It is not possible to distinguish by XPS the N atoms from TBA and from the protonated amine-terminated SAM. We crudely estimated the ratio TBA⁺/NH₃⁺ ensuring the global electrical neutrality as follows. A perfectly, closely packed, SAM of alkyl chains in Au surface has a maximum density of 4x10¹⁴ chain/cm² (or one alkyl chain per 25 Å²)¹⁰ and assuming a protonation at 30%, we estimated a density of 1.2x10¹⁴ NH₃⁺/cm². The most dense layer of POMs (sphere with a diameter of 1 nm) is a centered hexagonal geometry with a concentration of ~1.15x10¹⁴ POM/cm² (one POM per 86 Å²), thus about one NH₃⁺ per POM. In this ideal case, the neutrality requires 1 NH₃⁺ and 2 TBA⁺ counterions for PMo₁₂(O) or 3 TBA⁺ counterions for PMo₁₂(I), this TBA⁺/NH₃⁺ ratio could be lower for a less dense POM layer.

Section 3. Spectroscopic ellipsometry.

We recorded spectroscopic ellipsometry data (on *ca.* 1 cm² samples) in the visible range using a UVISSEL (Horiba Jobin Yvon) spectroscopic ellipsometer equipped with DeltaPsi 2 data analysis software. The system acquired a spectrum ranging from 2 to 4.5 eV (corresponding to 300–750 nm) with intervals of 0.1 eV (or 15 nm). The data were taken at an angle of incidence of 70°, and the compensator was set at 45°. We fit the data by a regression analysis to a film-on-substrate model as described by their thickness and their complex refractive indexes. First, a background for the substrate before monolayer deposition was recorded. We acquired three reference spectra at three different places of the surface spaced of few mm. Secondly, after the monolayer deposition, we acquired once again three spectra at three different places of the surface and we used a 2-layer model (substrate/SAM) to fit the measured data and to determine the SAM thickness. We employed the previously measured optical properties of the substrate (background), and we fixed the refractive index of the organic monolayer at 1.50.¹⁰ We note that a change from 1.50 to 1.55 would result in less than a 1 Å error for a thickness less than 30 Å. The three spectra measured on the sample were fitted separately using each of the three reference spectra, giving nine values for the SAM thickness. We calculated the mean value from this nine thickness values and the thickness uncertainty corresponding to the standard deviation. Overall, we estimated the accuracy of the SAM thickness measurements at ± 2 Å.¹¹

Section 4. AFM measurements.

TM-AFM.

Topographic images were acquired in tapping mode (TM) on an ICON (Bruker) microscope using a silicon tip (42 N/m spring constant, resonance frequency 320 kHz) at room temperature and in ambient condition. The AFM images were treated with the Gwyddion software.¹²

C-AFM.

Current–voltage characteristics were measured by conductive atomic force microscopy (Icon, Bruker), using Pt coated tip (RMN-12PT400B from Bruker, 0.3 N/m spring constant). To form the molecular junction, the conductive tip was located at a stationary contact point on the SAM surface at controlled loading force (~ 6-8 nN). The voltage was applied on the substrate, the tip is grounded via the input of the current-voltage preamplifier. The C-AFM tip is located at different places on the sample (typically on an array - 10x10 grid - of stationary contact points spaced of 50-100 nm), at a fixed loading force and the I–V characteristics were acquired directly by varying voltage for each contact point. The I-V characteristics were not averaged between successive measurements and typically up to 600 I-V measurements were acquired on each sample.

Loading force and C-AFM tip contact area.

The load force was set at \approx 6-8 nN for all the I-V measurements, a lower value leading to too many contact instabilities during the I-V measurements. Albeit larger than the usual load force (2-5 nN) used for CAFM on SAMs, this value is below the limit of about 60-70 nN at which the SAMs start to suffer from severe degradations. For example, a detailed study (Ref. 13) showed a limited strain-induced deformation of the monolayer (\leq 0.3 nm) at this used load force. The same conclusion was confirmed by our own study comparing mechanical and electrical properties of alkylthiol SAMs on flat Au surfaces and tiny Au nanodots.¹⁴

Data analysis.

Before to construct the current histograms and analyze the I-V curves with the one energy-level model and the TVS method, the raw set of I-V data is scanned and some I-V curves were discarded from the analysis:

- At high current, the I-V traces that reached the saturating current during the voltage scan (the compliance level of the trans-impedance amplifier, typically

5×10^{-9} A in Figs. S6, depending on the gain of the amplifier) and/or I-V traces displaying large and abrupt steps during the scan (contact instabilities).

- At low current, the I-V traces that reached the sensitivity limit (almost flat I-V traces and noisy I-Vs) and displayed random staircase behavior (due to the sensitivity limit - typically 0.1-1 pA depending on the used gain of the trans-impedance amplifier and the resolution of the ADC (analog-digital converter), Fig. S6).

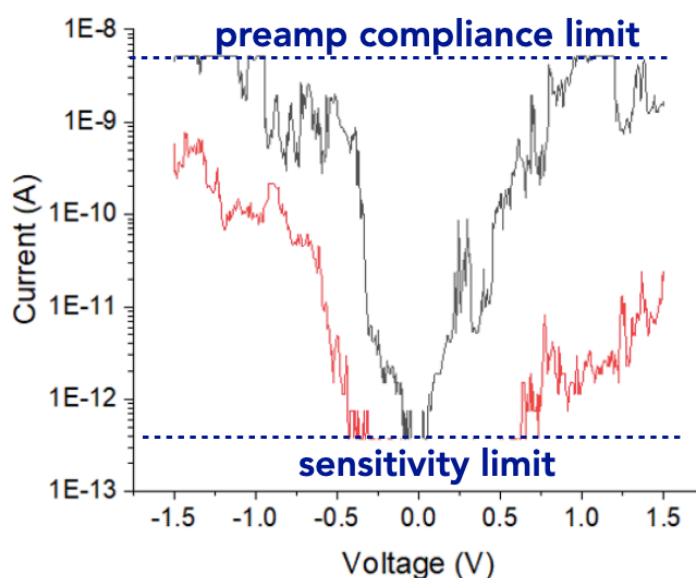


Figure S6. Typical examples of I-V curves discarded from the data analysis.

Fit of the single energy level (SEL) model.

All the I-V traces in Fig. 2 (main text) were fitted individually with the single energy-level (SEL) model (Eq. 1, main text) with 3 fit parameters: ϵ_{0-SEL} the energy position (with respect to the Fermi energy of electrodes) of the molecular orbital involved in the electron transport, Γ_1 and Γ_2 the electronic coupling energy between the molecules and the two electrodes. The fits (Figs. S7a and S7b) were

done with the routine included in ORIGIN software, using the method of least squares and the Levenberg Marquardt iteration algorithm.

The SEL model is a low temperature approximation albeit it can be used at room temperature for voltages below the resonant transport conditions^{15, 16} since the temperature broadening of the Fermi function is not taken into account. Moreover, a possible voltage dependence of $\epsilon_{0\text{-SEL}}$ is also neglected.¹⁷ It is known that the value of $\epsilon_{0\text{-SEL}}$ given by the fit of the SEL model depends on the voltage window used for the fit.¹⁵⁻¹⁷ This feature is confirmed (Fig. S8) showing that unreliable values are obtained with a too low voltage range (i.e. the SEL model is not reliable in the linear regime of the I-V curves) and not applicable when the voltage is high enough to bring the electrode Fermi energy close to molecular orbital (near resonant transport), here for a voltage window larger than -1.2/1.2V V where the fits are bad and the values of $\epsilon_{0\text{-SEL}}$ collapse. For voltage windows below -1V/1V we clearly see the lowering of $\epsilon_{0\text{-SEL}}$ by about 0.15-0.2 eV after reduction of the POMs. For comparison, the same mean \bar{I} -V curves are also analyzed by TVS (Fig. S7). We obtain a good agreement with the SEL model limiting the fit in the voltage window -1V/1V. For these reasons we limited the fits to a voltage window -1 V to 1 V to analyze the complete datasets shown in Fig. 2 (main text). To construct the histograms of the values of $\epsilon_{0\text{-SEL}}$, Γ_1 and Γ_2 (Fig. 4 in the main text), we discarded the cases for which the fits were not converging or not accurate enough (i.e. R-squared < 0.95). In the case of the reduced POM(I), the SEL model does not fit the data whatever the voltage window considered (Figs. S7 and S8), likely because the OM involved in the transport is too close to the Fermi energy (≈ 0.3 eV determined by TVS, Fig. S7), a situation where the model is not valid. Thus only the TVS method was used to analyze the I-V dataset in this latter case.

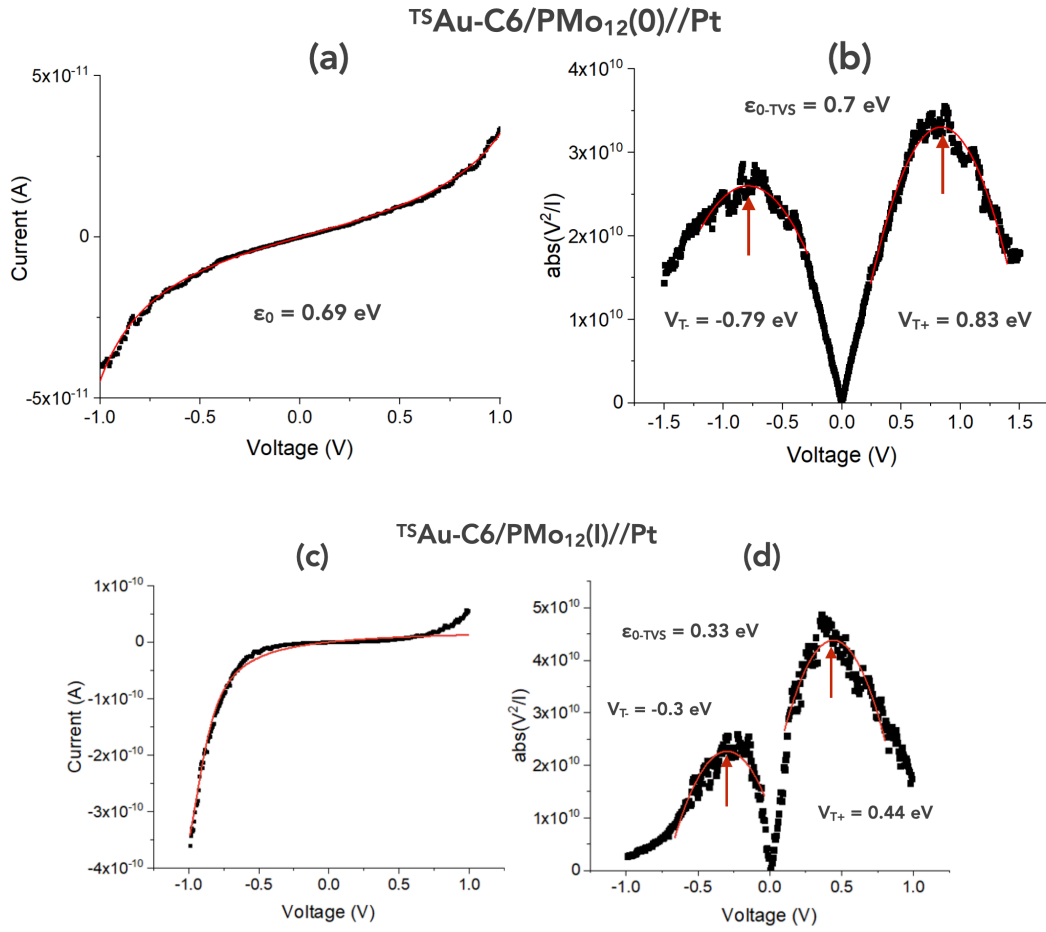


Figure S7. One energy-level model fits on the mean current-voltage curves within the bias voltage range $-1\text{V}/1\text{V}$ (solid red line) for (a) the ${}^{\text{TS}}\text{Au-C6/PMo}_{12}(\text{O})//\text{Pt}$ and (c) the ${}^{\text{TS}}\text{Au-C6/PMo}_{12}(\text{I})//\text{Pt}$ junctions. Typical TVS plots ($|V^2/I|$) vs. V for (b) the ${}^{\text{TS}}\text{Au-C6/PMo}_{12}(\text{O})//\text{Pt}$ and (d) the ${}^{\text{TS}}\text{Au-C6/PMo}_{12}(\text{I})//\text{Pt}$ junctions. The thresholds $V_{\text{T+}}$ and $V_{\text{T-}}$ are indicated by the vertical lines (with values) - max of a 2nd order polynomial function fitted around the max of the bell-shaped curves (to cope with noisy curves).

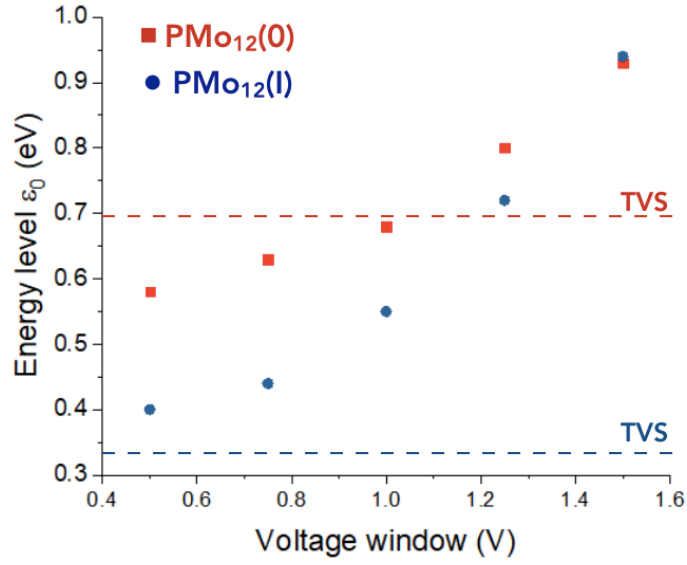


Figure S8. Values of ϵ_{0-SEL} obtained with the SEL model fitted on the mean \bar{I} - V curves for the $^{TS}\text{Au-C6}/\text{PMo}_{12}(\text{O})//\text{Pt}$ and $^{TS}\text{Au-C6}/\text{PMo}_{12}(\text{I})//\text{Pt}$ with increasing voltage windows (-0.5/0.5 V to -1.5/1.5 V) for the fits. The dashed lines indicate the value obtained by the TVS method (Fig. S7).

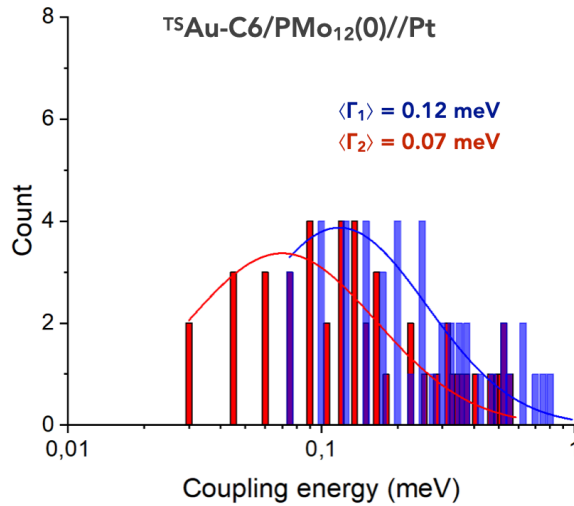


Figure S9. Distribution of the electrode coupling parameters Γ_1 and Γ_2 (SEL model) of the I - V data for the $^{TS}\text{Au}/\text{PMo}_{12}(\text{O})//\text{Pt}$ junctions (Fig. 2, main text) and log-normal fits of these distributions.

Section 5. Illumination setup.

We used a UV lamp (Analytic Jena) for UV light irradiation. This lamp has a wavelength centered at 302 nm (close to the absorbance peak, see Fig. S4) with a power of 0.5 mW/cm². The lamp was brought close (*ca.* few centimeters) to the sample in the CAFM setup.

Section 6. Redox cycles.

Figure S10 shows the 2D histograms of the same ^{TS}Au/PMo₁₂(O)//Pt junction (pristine) sequentially irradiated by UV light and let to relax in air at RT or under a moderate heating (hot plate, 80°C), the corresponding current histograms at -1V fitted by a log-normal distribution. The log-mean current ± the log-standard deviation is plotted in Fig. 3 (main text) versus the three sequences of photoreduction/relaxation. We note a degradation (lower currents) for the third cycle (data #6-8 in Figs. 3 and S10), albeit with a similar effect of the irradiation on the conductance. This degradation (lower currents than for the pristine sample) is observed whatever the reoxidation step (RT or heating at 80°C), while during the second cycle, the step at 80°C (data #5) returned the sample to almost the same current level as the pristine one. Thus the heating at 80°C is not specifically responsible to the sample degradation. Alkylthiol SAMs on Au are thermally stable up to 100-150°C,¹⁸ and up to ~200°C for PMo₁₂.¹⁹ Moreover, a thermal degradation (*e.g.* molecule desorption from the surface or thermal decomposition of the molecules) would have induced an increase of the current (less molecules in the SAMs and consequently a thinnest SAM, or even a direct contact between the C-AFM tip and the underlying Au substrate). This global decrease of the current (both for the reduced and oxidized samples) during the third cycle might be due to a drift of the loading force (*e.g.* a small decrease of the loading force), a pollution of the C-AFM tip or a pollution of the sample during the long duration of these measurements. A control measurement of the

SAM thickness (ellipsometry) after the three reduction/oxidation steps showed that thickness has increased by ~ 1 nm compared to the one of the pristine sample.

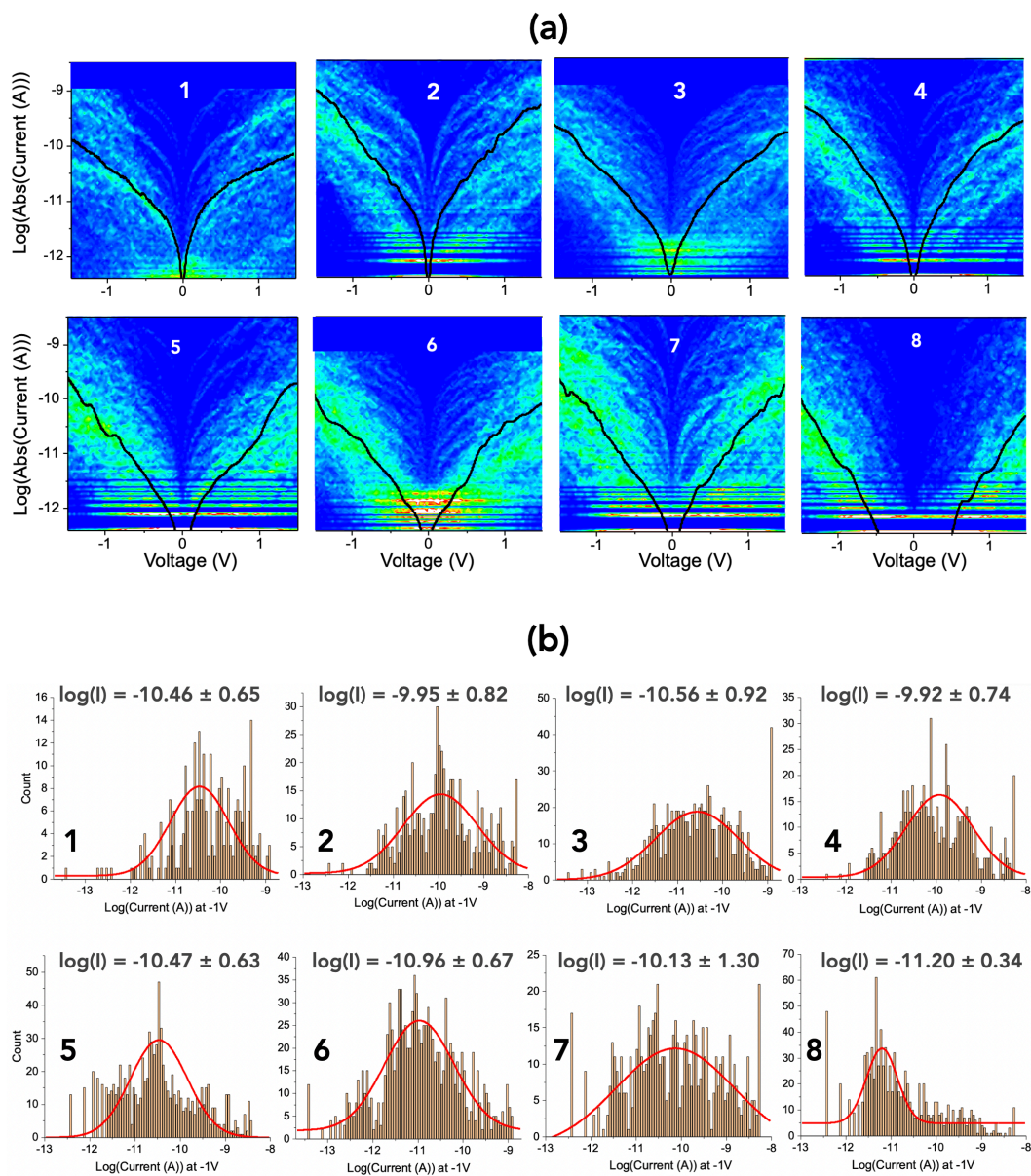


Figure S10. (a) 2D histograms of the I-V curves and (b) histograms of the current at -1V fitted by a log-normal distribution (the log-mean current and log-standard

deviation are given in the panels) for: 1) pristine, 2) UV 5.5h, 3) RT 14.5h, 4) UV 4h, 5) RT 24h, 6) UV 3.5h, 7) 80°C 2h.

In addition, the $\text{PMo}_{12}(\text{O})$ molecules were drop cast on a glass substrate and the film was UV irradiated in the same condition as the SAMs. The film turned from yellow-like to green-like (Fig. S11) indicating a partial reduction of the film (green = $\text{PMo}_{12}(\text{O})$ yellow + $\text{PMo}_{12}(\text{I})$ blue). It returns yellow-like after exposition in air, indicating the reversibility of the redox switching.

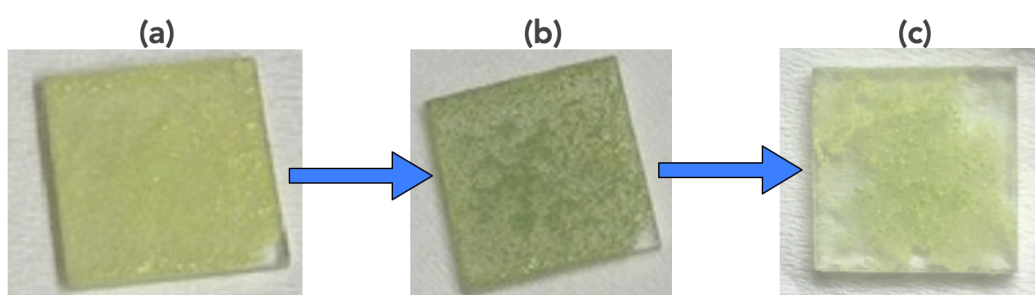


Figure S11. Pictures of a drop cast films (a) before, (b) after UV irradiation for 6 h and (c) after few days exposed at air.

Section 7. Machine learning and clustering.

Rationalized choice of the number of clusters.

To fix the optimized number of clusters, we analyzed the same dataset with various number of clusters from 2 to 6. Fig. S12 shows the obtained mean \bar{I} -Vs for the dataset of $^{\text{TS}}\text{Au-C6}/\text{PMo}_{12}(\text{O})//\text{Pt}$ junctions for 4, 5 and 6 clusters (the clusters are labeled cN/M, with N the cluster number by decreasing order of current amplitude and M the total number of clusters). In all cases, the cluster 1 corresponds to I-Vs saturating (current-voltage preamplifier compliance) during the measurements and this cluster is not considered further in the analysis. The mean \bar{I} -V curve of each cluster was analyzed with the SEL model and TVS method and the obtained MO energy levels are given in Table S1. Clearly, the solution

with 4 clusters (and less, not shown) is not satisfactory because the cluster $c_{3/4}$ can be decomposed (see the feature spaces in panels (a) and (b) in Fig. S12) in two clusters ($c_{3/5}$ and $c_{4/5}$) with significant differences: i) the mean \bar{I} -V curve of $c_{3/5}$ displays a negative asymmetry, while the cluster $c_{4/5}$ shows an almost symmetric mean \bar{I} -V curve (panel (e) in Fig. S12); ii) the ϵ_0 values (SEL and TVS) are different for $c_{3/5}$ than $c_{4/5}$ (see Table S1 and Table 3 in the main text), as well as the electronic coupling to the electrodes (Γ values, see Table 3 in the main text), while the values for the $c_{3/4}$ clusters are intermediate between those of the $c_{3/5}$ and $c_{4/5}$ clusters. Thus the analysis with 5 clusters is more pertinent. Extending to 6 clusters splits the cluster $c_{2/5}$ in two ($c_{2/6}$ and $c_{3/6}$, see feature spaces in panels (b) and (c) in Fig. S12, but the deduced ϵ_0 values (SEL and TVS) are similar (see Table S1), while the other clusters are not modified by extending to 6 clusters (Figs. S12 and Table S1: $c_{3/5} \equiv c_{4/6}$, $c_{4/5} \equiv c_{5/6}$ and $c_{5/5} \equiv c_{6/6}$). Thus using 6 clusters does not add more pertinent information and we conclude that the analyze with 5 clusters is the optimized approach.

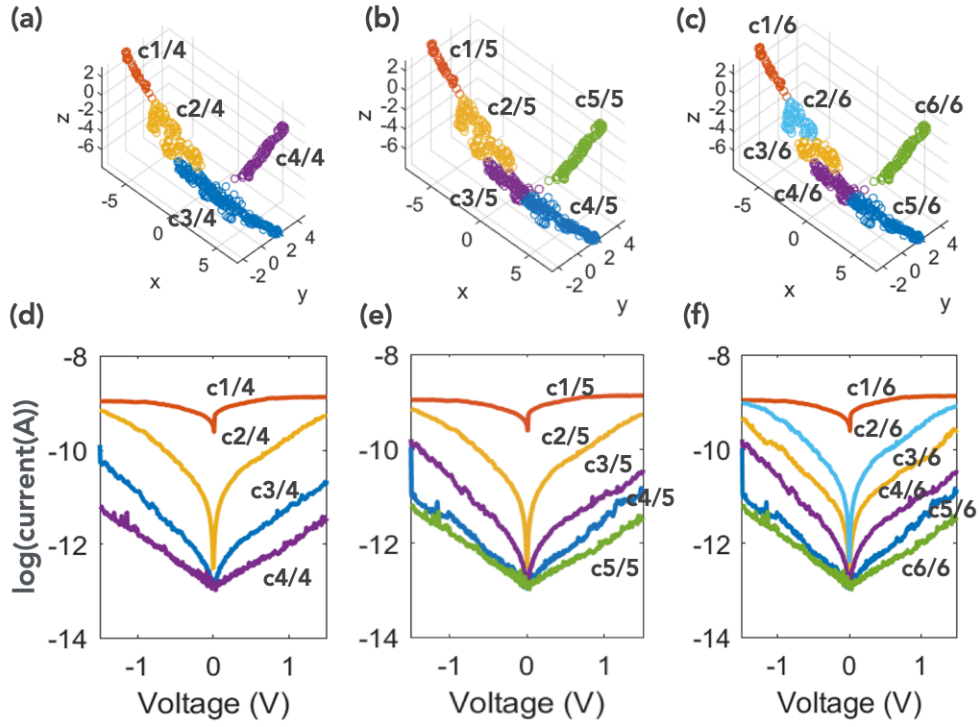


Figure S12. $^{75}\text{Au-C6-PMo}_{12}(0)//\text{Pt}$ junction dataset. (a-c) feature spaces for 4, 5 and 6 clusters, respectively. (d-f) Mean \bar{I} -V for 4, 5 and 6 clusters, respectively.

4 clusters	$\epsilon_{0\text{-SEL}}$ (eV)	$\epsilon_{0\text{-TVS}}$ (eV)	5 clusters	$\epsilon_{0\text{-SEL}}$ (eV)	$\epsilon_{0\text{-TVS}}$ (eV)	6 clusters	$\epsilon_{0\text{-SEL}}$ (eV)	$\epsilon_{0\text{-TVS}}$ (eV)
c2/4	0.69	0.65	c2/5	0.69	0.61	c2/6	0.69	0.65
						c3/6	0.70	0.64
c3/4	0.64	0.57	c3/5	0.67	0.60	c4/6	0.66	0.60
			c4/5	0.60	0.55	c5/6	0.60	0.54
c4/4	0.80	0.68	c5/5	0.81	0.72	c6/6	0.80	0.70

Table S1. Energy of the MO determined by the SEL model and the TVS method (on the mean \bar{I} -V, Figs. S12, S14 and S15) for the clustering analysis with 4, 5 and 6 clusters. The light gray lines highlight the pertinent clusters.

The same analysis conducted with the dataset of $^{75}\text{Au-C6-PMo}_{12}(\text{I})//\text{Pt}$ junctions (Fig. S13 and Table S2) leads to the same conclusion. The clusters $c2/M$ and $c3/M$ are identical whatever the total number M of clusters (Fig. S13 and Table S2) and the clusters $c3/6$ and $c4/6$ (analysis with 6 clusters) are identical and thus this splitting is not useful. Comparing the 4 and 5 clusters analysis, the cluster $c4/4$ can be decomposed in two clusters $c4/5$ and $c5/5$ (Fig. S13) with slightly different parameters (Table S2 and Table 3 in the main text). Thus we also keep an optimized number of 5 clusters for the analysis of the $^{75}\text{Au-C6-PMo}_{12}(\text{I})//\text{Pt}$ junction dataset. This is also consistent for comparison with the analysis of the $^{75}\text{Au-C6-PMo}_{12}(\text{O})//\text{Pt}$ junction dataset.

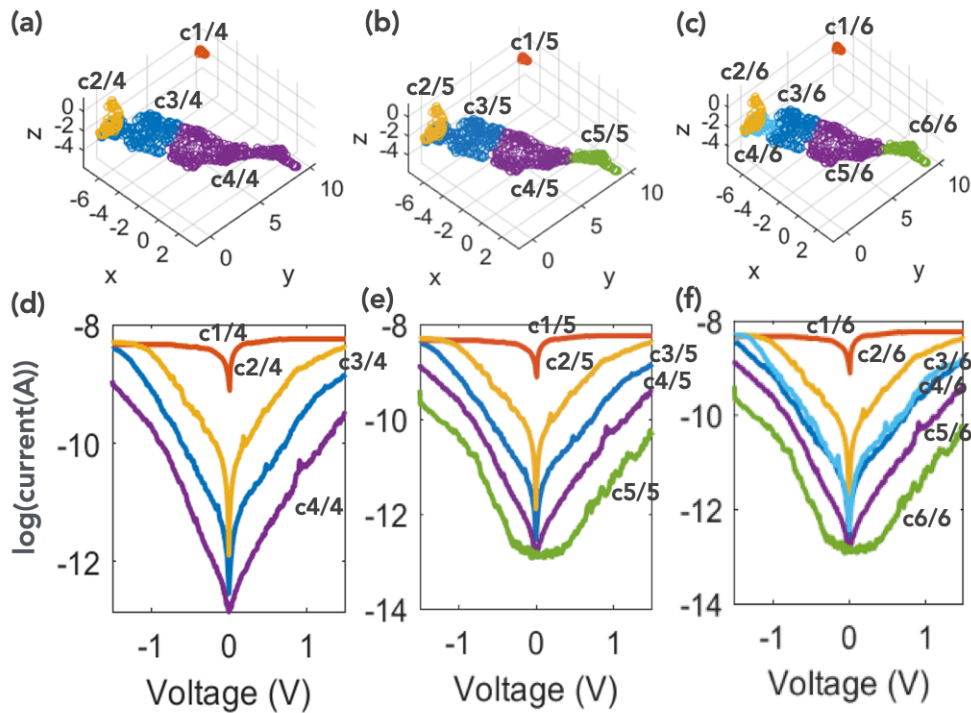


Figure S13. $^{75}\text{Au-C6-PMo}_{12}(\text{I})//\text{Pt}$ junction dataset. (a-c) feature spaces for 4, 5 and 6 clusters, respectively. (d-f) Mean \bar{I} -V for 4, 5 and 6 clusters, respectively.

4 clusters	$\epsilon_{0-TV\bar{S}}$ (eV)	5 clusters	$\epsilon_{0-TV\bar{S}}$ (eV)	6 clusters	$\epsilon_{0-TV\bar{S}}$ (eV)
c2/4	0.41	c2/5	0.43	c2/6	0.41
c3/4	0.36	c3/5	0.38	c3/6	0.37
				c4/6	0.38
c4/4	0.29	c4/5	0.33	c5/6	0.28
		c5/5	0.28	c6/6	0.26

Table S2. Energy of the MO determined by the TVS method (on the mean \bar{I} -V, Figs. S13, S19 and S20) for the clustering analysis with 4, 5 and 6 clusters. The light gray lines highlight the pertinent clusters.

Statistical analysis of the clusters.

In this section, we present the detailed analysis of the I-V curves in the case of 5 clusters. The cluster 1 (corresponding to I-Vs at the saturation limit of the C-AFM apparatus) is not considered.

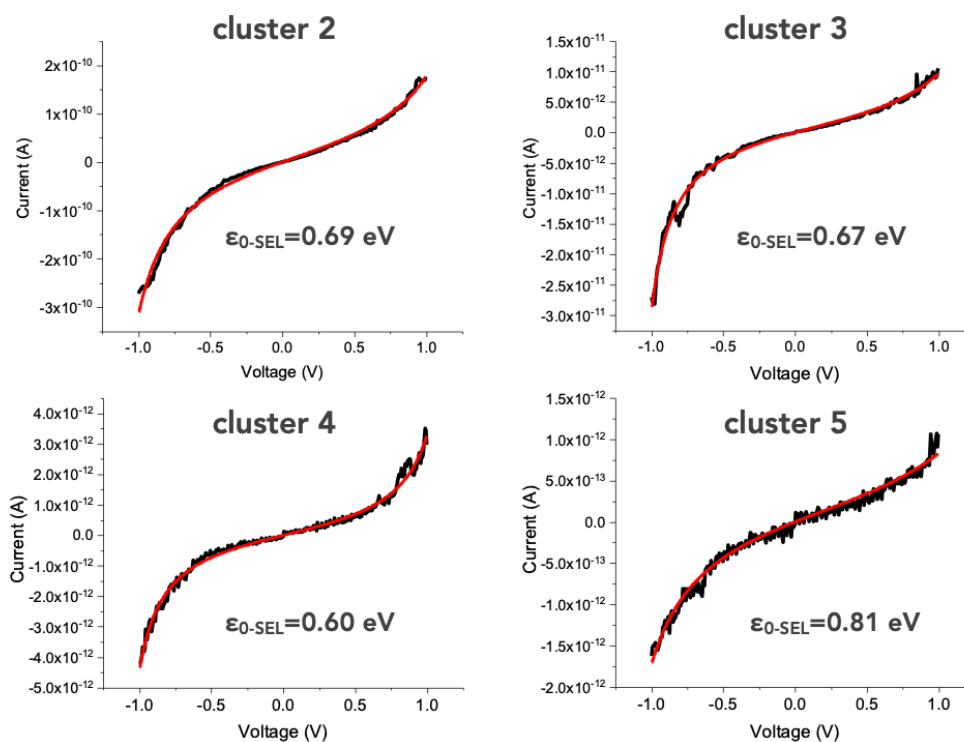


Figure S14. SEL fit (on mean \bar{I} -V) of the four clusters of the $^{75}\text{Au-C6/PMo}_{12}(0)//\text{Pt}$ devices.

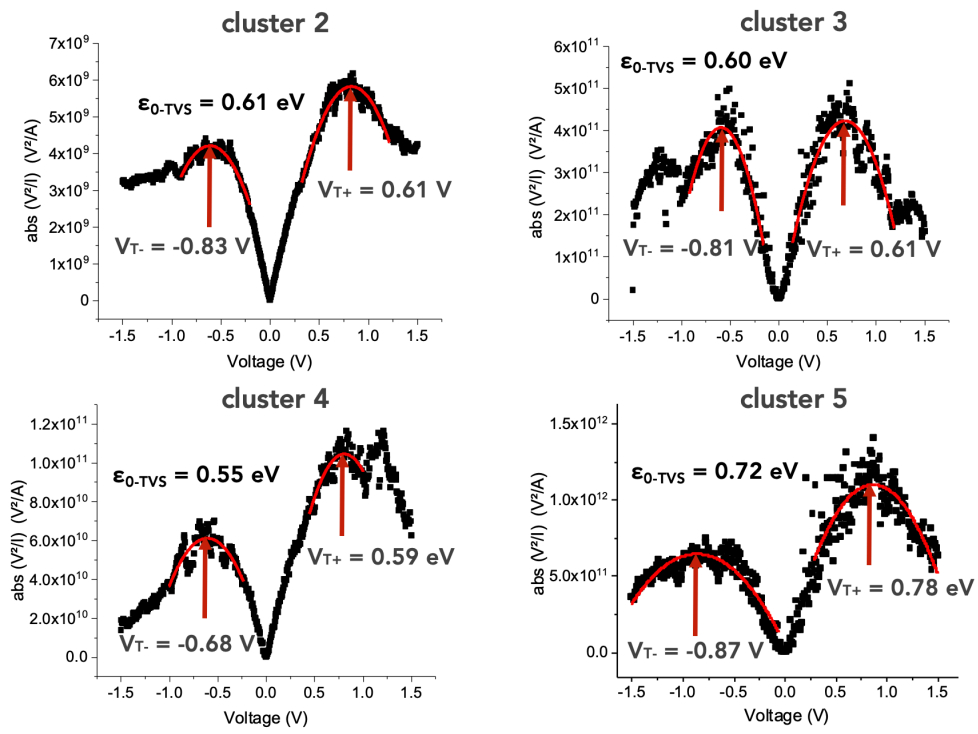


Figure S15. TVS analysis of the mean \bar{I} - V of the four clusters of the $^{TS}\text{Au-C6}/\text{PMo}_{12}(\text{O})//\text{Pt}$ devices (same data as Fig. S14).

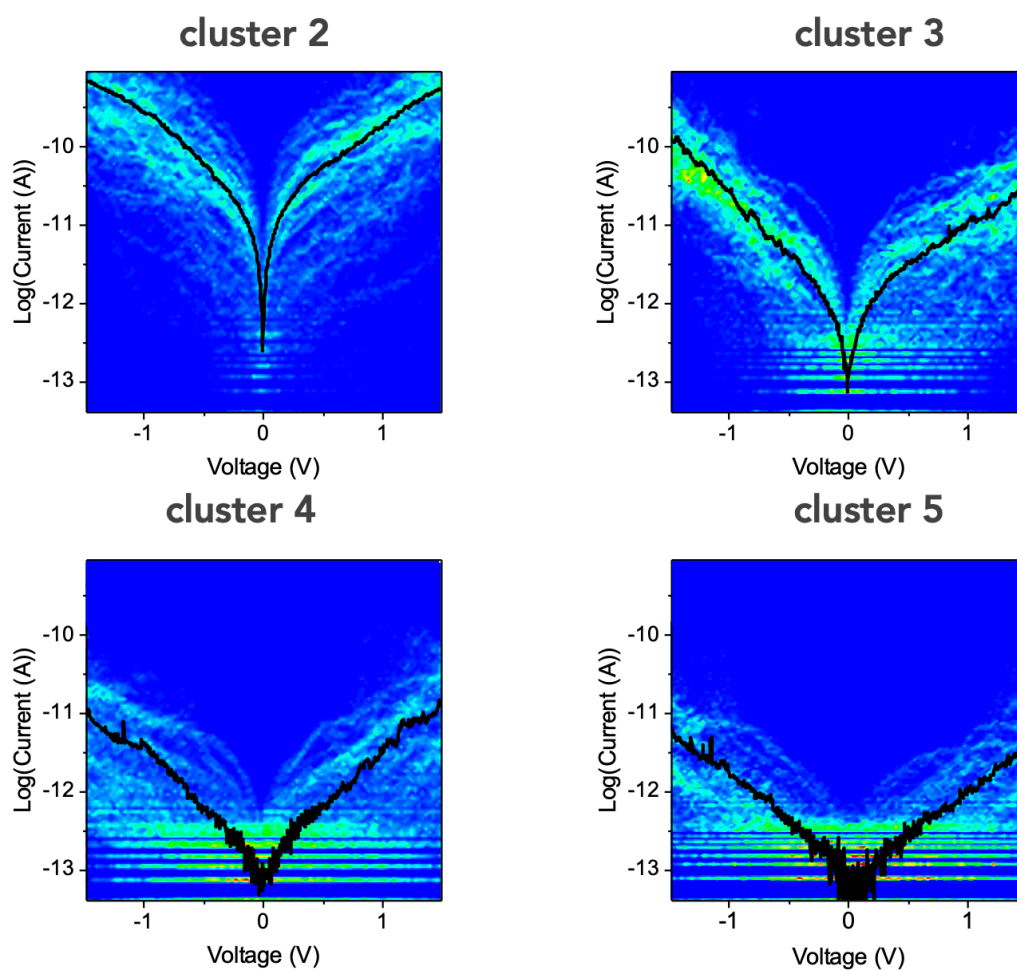


Figure S16. Current-voltage (I - V) curves of the $^{75}\text{Au-C6/PMo}_{12}(\text{O})//\text{Pt}$ junctions belonging to each cluster with the mean \bar{I} - V curve (dark lines). The numbers of I - V s are 134 (cluster 2), 102 (cluster 3), 159 (cluster 4) and 107 (cluster 5).

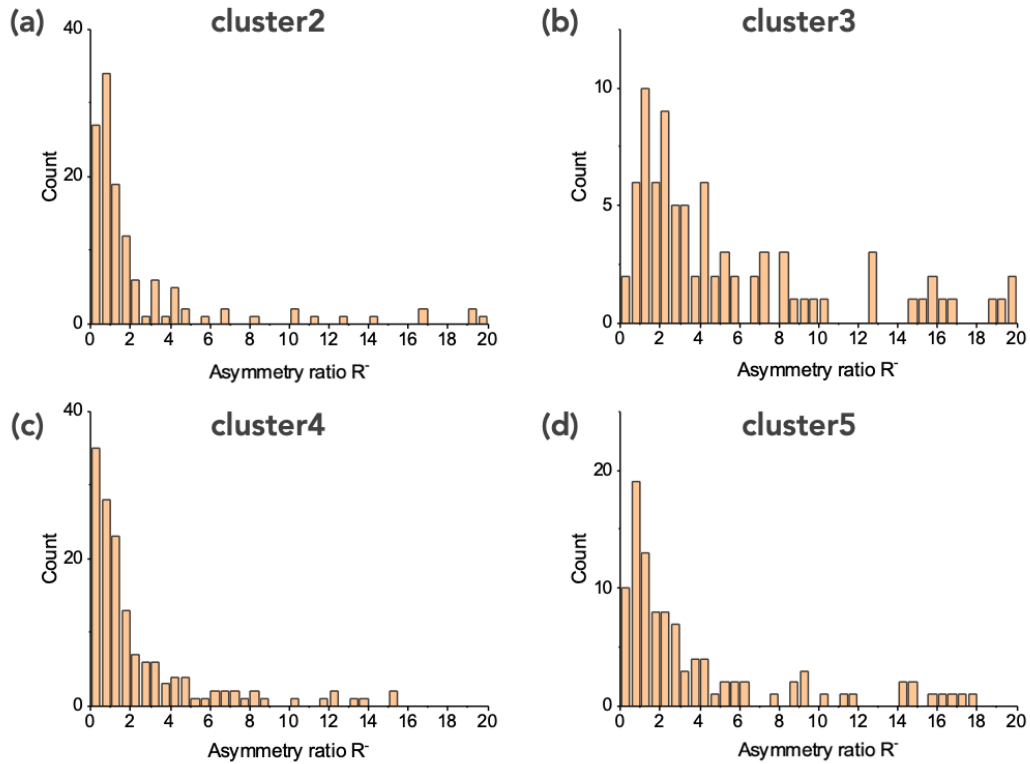


Figure S17. Histograms of the asymmetry ratios $R = I(-1.5V)/I(1.5V)$ calculated from all the individual I-Vs belonging to each cluster of the $^{TS}Au-C6/PMo_{12}(O)//Pt$ junctions shown in Fig. S16.

The histograms of the asymmetry ratio of the $^{TS}Au-C6/PMo_{12}(O)//Pt$ junctions (Fig. S17) confirm the analysis from the mean \bar{I} -V curves (Table 3 main text) that the cluster 3 contains a majority of I-V curves with an asymmetry ratio larger than 2 (71% of the data), while the 3 other clusters have more than 50% of almost symmetric I-V ($R < 2$: 72% for the cluster 2, 66 % for the cluster 4 and 50% for the cluster 5).

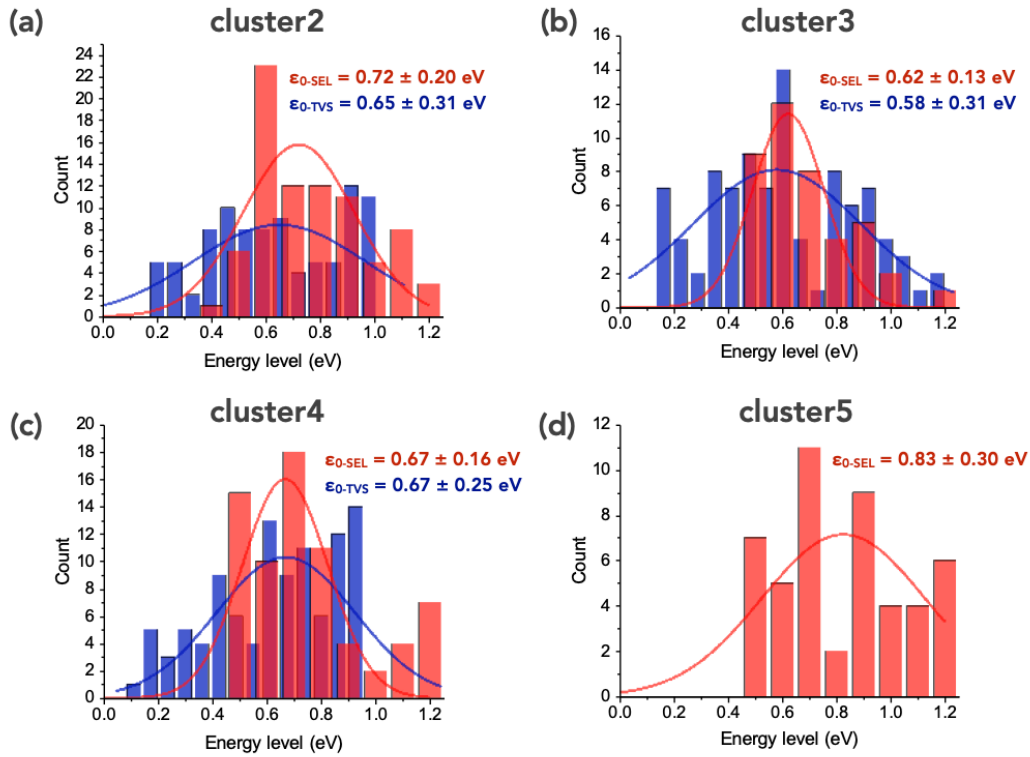


Figure S18. Histograms of the energy levels $\epsilon_{0\text{-SEL}}$ and $\epsilon_{0\text{-TVS}}$ obtained with the SEL model and TVS method for all the individuals I-Vs belonging to each cluster of the ${}^{\text{TS}}\text{Au-C6/PMo}_{12}(0)//\text{Pt}$ junctions shown in Fig. S16. Solid lines are the fits by a Gaussian distribution with the mean value of the energy level \pm standard deviation indicated in the panels.

The Gaussian fits of distributions of the $\epsilon_{0\text{-SEL}}$ and $\epsilon_{0\text{-TVS}}$ values obtained for each cluster (Fig. S18, and Table S3) confirm the value directly obtained from the mean \bar{I} -V curves (Figs. S14, S15) and are compared in Table S3 for convenience. The TVS method for cluster 5 gives a large distribution of value, likely due to the fact that many I-Vs in this cluster are noisy curves at the sensitivity limit of the C-AFM system and they were discarded in this case.

	$^{TS}\text{Au-C6/PMo}_{12}(\text{O})//\text{Pt}$				$^{TS}\text{Au-C6/PMo}_{12}(\text{I})//\text{Pt}$			
cluster	C2 (24.6%)	C3 (18.8%)	C4 (29.2%)	C5 (19.7%)	C2 (12.5%)	C3 (35.7%)	C4 (35.5%)	C5 (13.5%)
$\epsilon_{0\text{-TVS}}$ (eV) mean \bar{I} -V	0.61	0.60	0.55	0.72	0.43	0.38	0.33	0.28
$\epsilon_{0\text{-TVS}}$ (eV) histogram	0.65	0.58	0.67	n.a.	0.45	0.34	0.35	n.a.
$\epsilon_{0\text{-SEL}}$ (eV) mean \bar{I} -V	0.69	0.67	0.60	0.81	n.a.			
$\epsilon_{0\text{-SEL}}$ (eV) histogram	0.72	0.62	0.67	0.83				

Table S3. Comparison of the energy level ϵ_0 for the TVS method and the SEL model deduced from the mean \bar{I} -V curves (Figs. S14, S15, S19) and from Gaussian fits of the histograms belonging to the different clusters (Figs. S18 and S23).

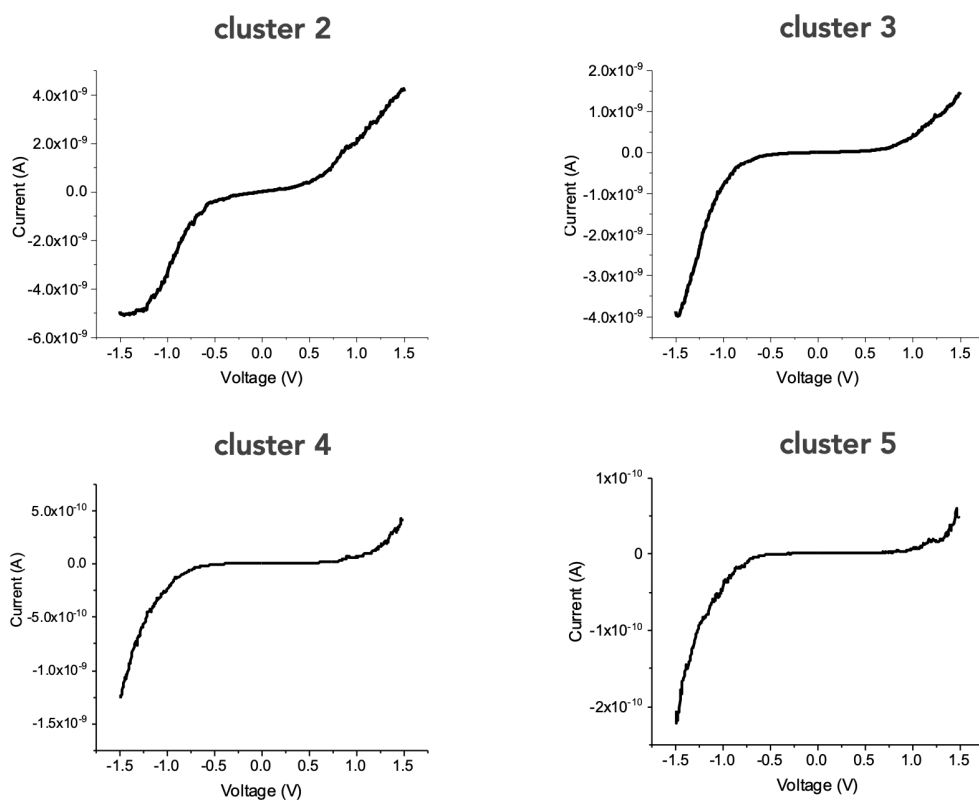


Figure S19. Mean \bar{I} -V of the four clusters of the $^{TS}\text{Au-C6/PMo}_{12}(\text{I})//\text{Pt}$ devices.

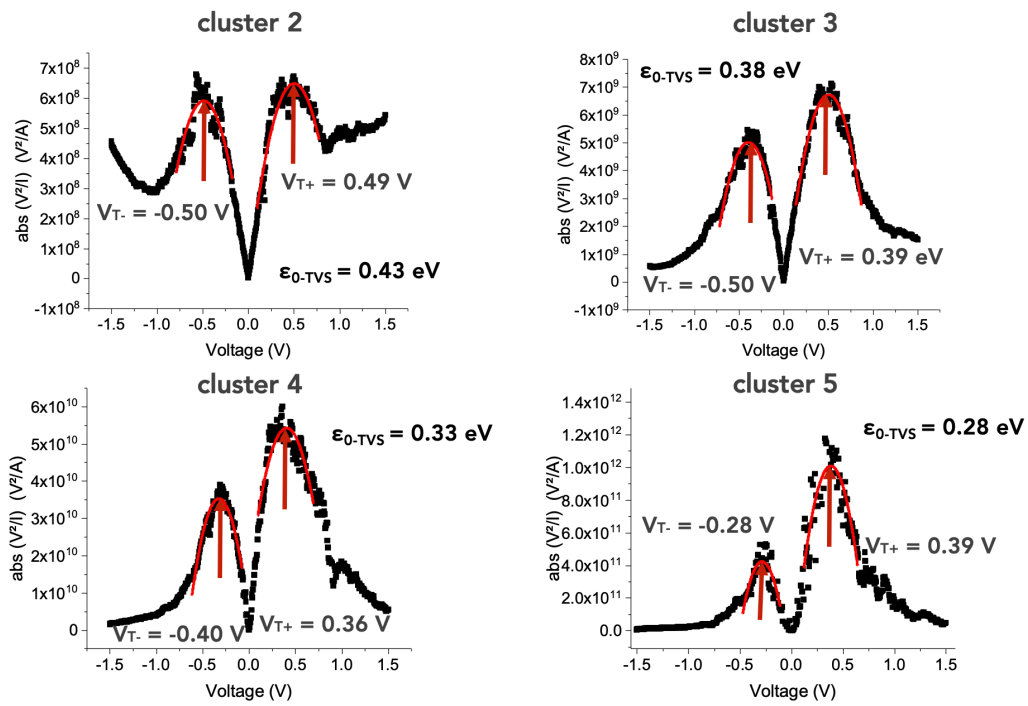


Figure S20. TVS analysis of the mean \bar{I} -V of the four clusters of the $^{TS}\text{Au-C6}/\text{PMo}_{12}(\text{I})//\text{Pt}$ devices (same data as Fig. S19).

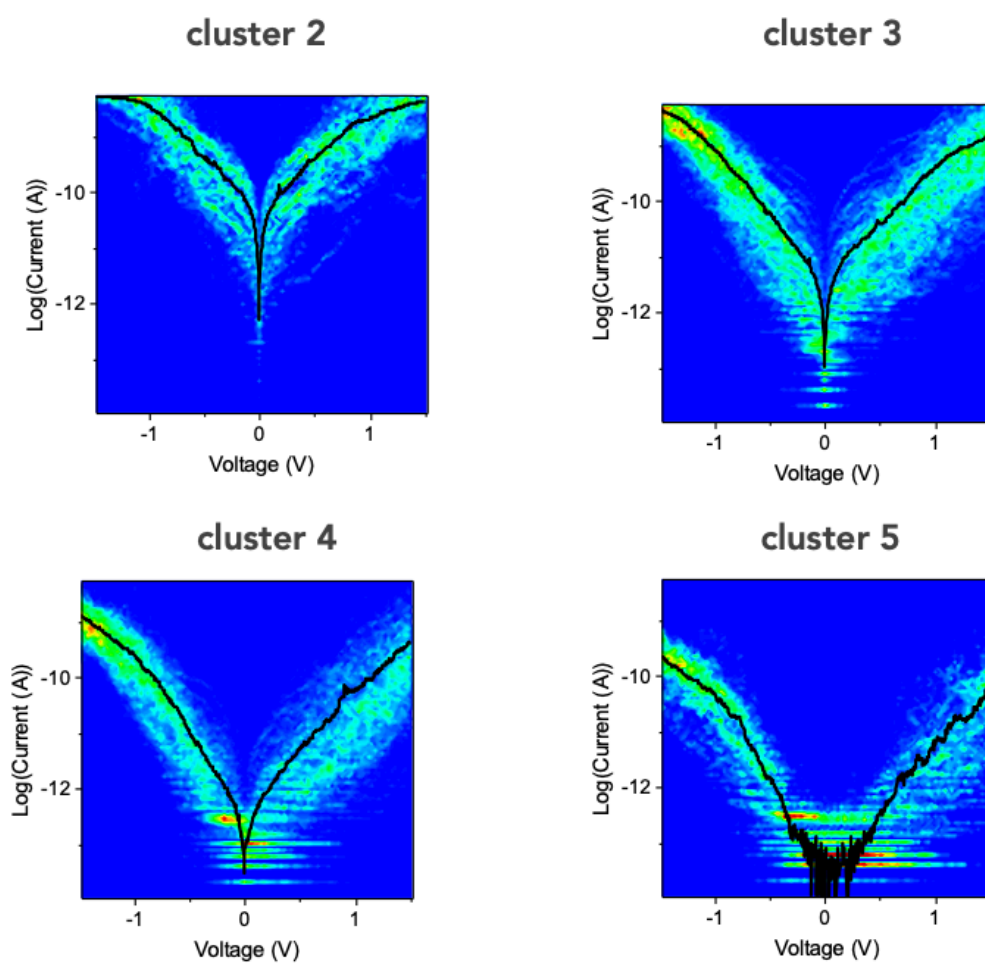


Figure S21. Current-voltage (I - V) curves of the $^{75}\text{Au-C6/PMo}_{12}(\text{I})//\text{Pt}$ junctions belonging to each cluster with the mean \bar{I} - V curve (in red). The numbers of I - V s are 75 (cluster 2), 214 (cluster 3), 213 (cluster 4) and 81 (cluster 5).

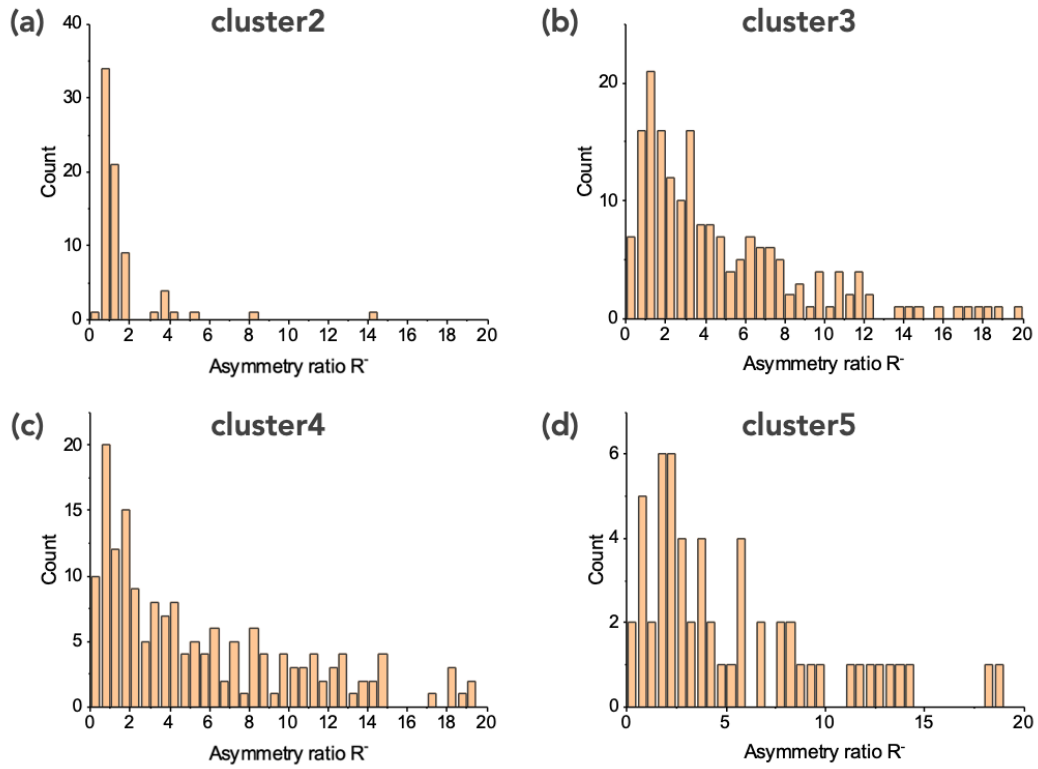


Figure S22. Histograms of the asymmetry ratios $R = I(-1.5V)/I(1.5V)$ calculated from all the individual I-Vs belonging to each cluster of the $^{75}\text{Au-C6}/\text{PMo}_{12}(\text{I})//\text{Pt}$ junctions shown in Fig. S21.

The histograms of the asymmetry ratio (Fig. S22) confirm the analysis from the mean \bar{I} -V curves (Table 3 main text) that all the clusters for $^{75}\text{Au-C6}/\text{PMo}_{12}(\text{I})//\text{Pt}$ junctions contain a majority of I-V ($\approx 70\%$ of the data) with an asymmetry ratio larger than 2 (68% for the cluster 3, 67 % for the cluster 4 and 74% for the cluster 5). Note that, as for the analysis from the mean \bar{I} -V curve, the ratio for the cluster 2 is not meaningful since almost all the I-Vs saturate (compliance of the preamplifier of the C-AFM apparatus) at voltage ± 1.5 V(Fig. S21).

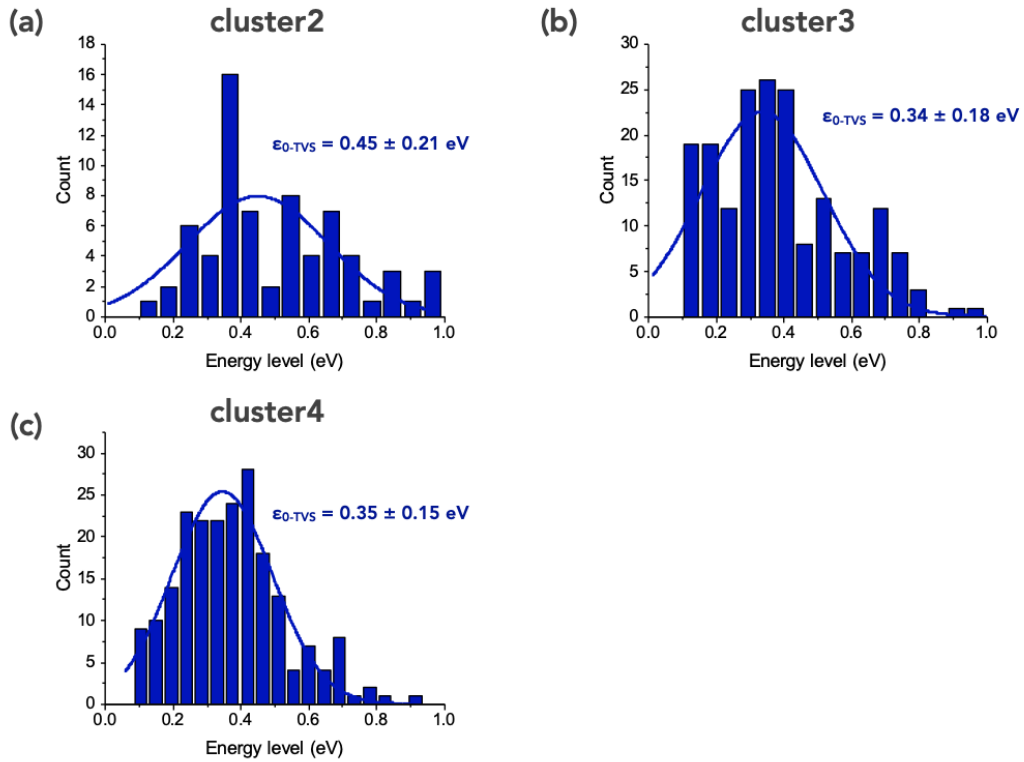


Figure S23. Histograms of the energy levels ϵ_{0-TV_S} obtained with TVS method for all the individuals I-Vs belonging to each cluster of the ${}^{TS}\text{Au-C6/PMo}_{12}(\text{I})//\text{Pt}$ junctions shown in Fig. S21.

The histograms of ϵ_{0-TV_S} values (TVS analysis) conducted for each cluster (Fig. S23, and Table S3) confirm the value directly obtained from the mean \bar{I} -V curve (Figs. S19, S20) and are compared in Table S3 for convenience. The TVS method for the cluster 5 gives a large distribution of value, likely due to the fact that many I-Vs in this cluster are noisy curves at the sensitivity limit of the C-AFM system and was discarded in this case.

Section 8. References samples, C6 SAMs.

Figure S24a shows the I-V dataset (415 I-Vs) measured by C-AFM on ${}^{TS}\text{Au-C6}//\text{Pt}$ samples. The fit by the SEL model and the TVS method on the mean \bar{I} -V give ϵ_{0-SEL}

= 0.85 eV (Fig. S24b) and $\epsilon_{0-TV\text{S}} = 0.72$ eV (Fig. S24c). The statistical analysis of the complete data set gives almost the same mean value of ~ 0.9 eV for both methods (Fig. S24d). This latter value is in good agreement with the energy position of the LUMO for alkyl chains on Au.^{20, 21}

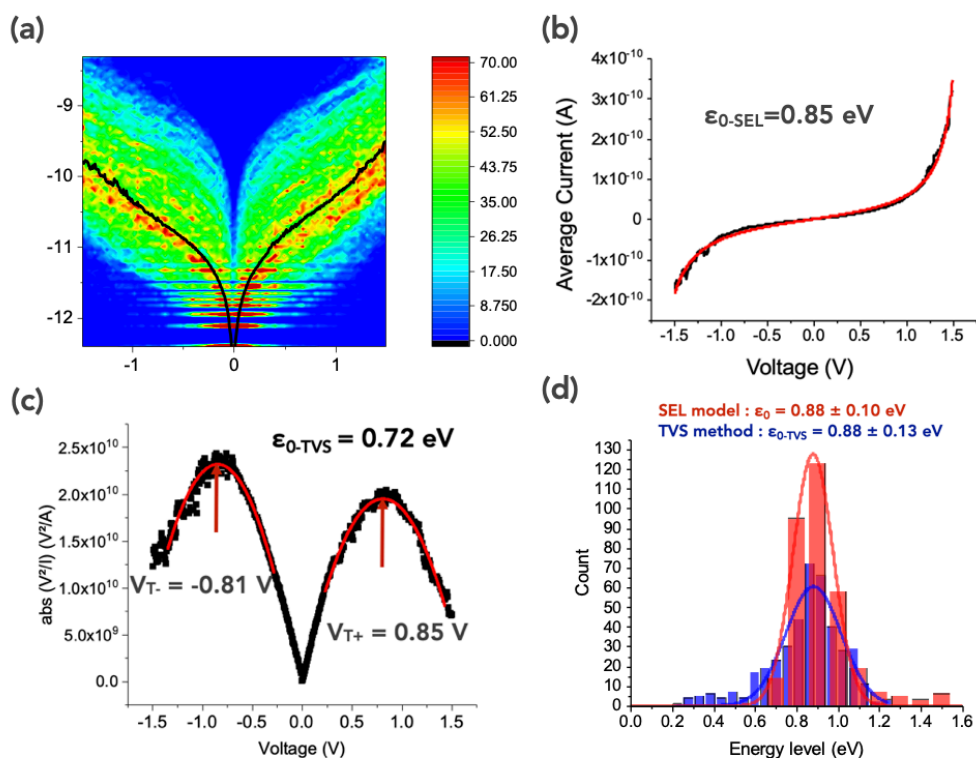


Figure S24. (a) 2D histogram of 415 I-Vs of $^{TS}\text{Au-C6//Pt}$ junction, and mean current \bar{I} -V curve (dark line), (b) typical fit of the SEL model and (c) TVS method on the mean \bar{I} -V, (d) statistical distribution of the energy level and fit with a Gaussian distribution.

References

1. C. Rocchiccioli-Deltcheff, M. Fournier, R. Franck and R. Thouvenot, *Inorganic Chemistry*, 1983, **22**, 207-216.

2. V. Artero and A. Proust, *European Journal of Inorganic Chemistry*, 2000, **2000**, 2393-2400.
3. N. Elgrishi, M. B. Chambers, X. Wang and M. Fontecave, *Chem Soc Rev*, 2017, **46**, 761-796.
4. D. A. Shirley, *Phys. Rev. B*, 1972, **5**, 4709-4714.
5. J. F. Moulder, *Handbook of X-ray Photoelectron Spectroscopy: A Reference Book of Standard Spectra for Identification and Interpretation of XPS Data*, Physical Electronics Division, Perkin-Elmer Corporation., 1992.
6. M. Hegner, P. Wagner and G. Semenza, *Surf. Sci.*, 1993, **291**, 39-46.
7. E. Weiss, R. Chiechi, G. Kaufman, J. Kriebel, Z. Li, M. Duati, M. Rampi and G. Whitesides, *J. Am. Chem. Soc.*, 2007, **129**, 4336-4349.
8. E. A. Weiss, G. K. Kaufman, J. K. Kriebel, Z. Li, R. Schalek and G. M. Whitesides, *Langmuir*, 2007, **23**, 9686-9694.
9. K. Dalla Francesca, S. Lenfant, M. Laurans, F. Volatron, G. Izzet, V. Humblot, C. Methivier, D. Guerin, A. Proust and D. Vuillaume, *Nanoscale*, 2019, **11**, 1863-1878.
10. A. Ulman, *An introduction to ultrathin organic films : from Langmuir-Blodgett to Self-assembly*, Academic press, Boston, 1991.
11. J. P. Rabe and W. Knoll, *Optics Communications*, 1986, **57**, 189-192.
12. D. Necas and P. Klapetek, *Central European Journal of Physics*, 2012, **10**, 181-188.
13. V. B. Engelkes and C. Daniel Frisbie, *The Journal of Physical Chemistry B*, 2006, **110**, 10011-10020.
14. K. Smaali, S. Desbief, G. Foti, T. Frederiksen, D. Sanchez-Portal, A. Arnau, J. P. Nys, P. Leclere, D. Vuillaume and N. Clement, *Nanoscale*, 2015, **7**, 1809-1819.
15. L. Grüter, F. Cheng, T. T. Heikkilä, M. T. González, F. Diederich, C. Schönenberger and M. Calame, *Nanotechnology*, 2005, **16**, 2143-2148.
16. J. Brunner, Basel University, 2013.

17. V. Delmas, V. Diez-Cabanes, C. Van Dyck, E. Scheer, K. Costuas and J. Cornil, *Physical Chemistry Chemical Physics*, 2020, **22**, 26702-26706.
18. C. Vericat, M. E. Vela, G. Benitez, P. Carro and R. C. Salvarezza, *Chem Soc Rev*, 2010, **39**, 1805-1834.
19. M. M. M. Abd El-Wahab and A. A. Said, *Journal of Molecular Catalysis A: Chemical*, 2005, **240**, 109-118.
20. Y. Qi, O. Yaffe, E. Tirosh, A. Vilan, D. Cahen and A. Kahn, *Chemical Physics Letters*, 2011, **511**, 344-347.
21. G. Ricoeur, S. Lenfant, D. Guerin and D. Vuillaume, *Journal of Physical Chemistry C*, 2012, **116**, 20722-20730.